Journal of Colloid and Interface Science 561 (2020) 501–511

Contents lists available at ScienceDirect

Journal of Colloid and Interface Science

journal homepage: www.elsevier.com/locate/jcis

A "bottle-around-ship" like method synthesized yolk-shell Ag_3PO_4@MIL-53(Fe) Z-scheme photocatalysts for enhanced tetracycline removal

Xiaopei Li [a,1], Zhuotong Zeng [b,1], Guangming Zeng [a,*], Dongbo Wang [a,*], Rong Xiao [b,*], Yingrong Wang [a], Chenyun Zhou [a], Huan Yi [a], Shujing Ye [a], Yang Yang [a], Weiping Xiong [a]

[a] College of Environmental Science and Engineering, Hunan University and Laboratory of Environmental Biology and Pollution Control (Hunan University), Ministry of Education, Changsha 410082, PR China
[b] Department of Dermatology, Second Xiangya Hospital, Central South University, Changsha 410011, PR China

GRAPHICAL ABSTRACT

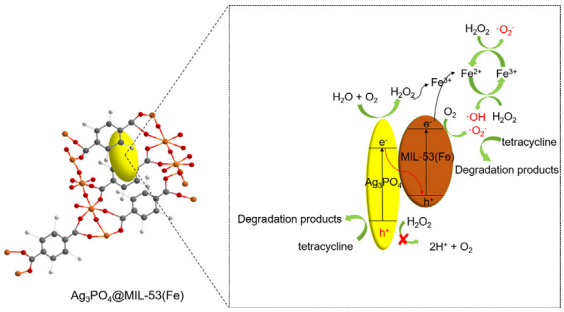

ARTICLE INFO

Article history:
Received 29 August 2019
Revised 24 October 2019
Accepted 7 November 2019
Available online 8 November 2019

Keywords:
Ag_3PO_4
MIL-53(Fe)
Yolk-shell structure
Z-scheme photocatalyst
Tetracycline

ABSTRACT

A novel yolk-shell Ag_3PO_4@MIL-53(Fe) Z-scheme photocatalyst was fabricated via a "bottle-around-ship" like method. Experiments on the treatment of tetracycline upon visible light irradiation showed that the as-prepared photocatalyst possessed excellent photocatalytic performance. Experimental results showed that tetracycline removal efficiency of the yolk-shell Ag_3PO_4@MIL-53(Fe) Z-scheme photocatalyst was almost 3 times higher than that of MIL-53(Fe). The enhanced photocatalytic performance of Ag_3PO_4@MIL-53(Fe) nanocomposite could be contributed to its higher surface area, better absorption capability, and greater charge separation efficiency. In addition, the H_2O_2 concentration detection results for Ag_3PO_4 (154 μmol/L) and Ag_3PO_4@MIL-53(Fe) (52 μmol/L) indicated that a big part of generated H_2O_2 on the Ag_3PO_4 core would be quickly decomposed by the MIL-53(Fe) shell and generated more reactive species through the photo-Fenton-like reaction, which is beneficial for the improvement of photocatalytic performance. This is a promising approach to fabricate yolk-shell structure photocatalyst and a different aspect to design multiple semiconductor composites heterojunction for environmental remediation.

1. Introduction

With the development of the time, the use of antibiotics has increased sharply, which not only damages the ecosystem, but also poses a threat to human health. It is urgent to remove antibiotic

* Corresponding authors.
E-mail addresses: zgming@hnu.edu.cn (G. Zeng), dongbowang@hnu.edu.cn (D. Wang), xiaorong65@csu.edu.cn (R. Xiao).
[1] These authors contribute equally to this article.

https://doi.org/10.1016/j.jcis.2019.11.025
0021-9797/

pollutants from the environment [1–10]. For instance, tetracycline (TC), one of extensively used antibiotics, which is hardly to be metabolized by human beings or animals, and could accumulate in the natural environment at significant levels. For example, the maximum concentration of TC in Yangtze River, China was 312 ng/g, while the minimum detection concentration of TC was 100 ng/g [11]. Owing to its chemical stability and antibacterial nature, it is difficult to be removed by traditional wastewater treatment. Thus, effective removal of TC in the environment is imperative [12]. Various methods were tested to solve this problem in the past, such as membrane filtration [13], adsorption [14], Fenton-reaction [15], and photocatalysis [16–20]. Among them, photocatalysis has gained significant attention on account of its low cost, low toxicity, and superb degradation efficiency [21–24].

Metal-organic frameworks (MOFs) was constituted by straightforward self-assembly of metal ions or clusters with organic linkers [25,26]. MOF materials offer an ideal platform for rationally combined light-harvesting components and catalytic activity centers in one system and shows better performance [27]. Hence, MOF materials could be considered as photocatalysts with unlimited potential. Among numerous MOF materials, MIL-53(Fe) has gained extensive interests in the fields of hydrogen generation, catalysis, drug delivery, and gas storage [28–31]. The Fe-O clusters could be activated upon visible light irradiation, which makes MIL-53 (Fe) available for visible light photocatalysis. However, owing to its high recombination rate of photoinduced carriers, MIL-53(Fe) shows unsatisfied photocatalytic performance.

To solve this problem, constructing a Z-scheme heterostructure seems to be a feasible way. Among various Ag-based materials, Ag_3PO_4 is a type of photocatalyst which possesses superior photo-oxidation capability [32–35]. However, owing to the limit by its conduction band position (0.45 eV vs. normal hydrogen electrode (NHE), pH = 0), the photogenerated electrons of Ag_3PO_4 could be absorbed by Ag^+ released from the lattice of Ag_3PO_4 ($4Ag_3PO_4 + 6H_2O + 12\,h^+ + 12e^- \rightarrow 2Ag + 4H_3PO_4 + 3O_2$), instead of H_2O if there were no scavengers being existed. In addition, it is uneconomical that using pure Ag_3PO_4 for the degradation of pollutants or splitting water for O_2 due to the existence of noble material silver.

Previous publications demonstrated that nanoparticles could be surrounded by MOFs via "bottle-around-ship" approach [36]. In addition, plenty of Ag_3PO_4@MOF composites was proven to be efficient photocatalysts for various applications [37–43]. This enlightened us to introduce a small amount of Ag_3PO_4 into MIL-53(Fe) through "bottle-around-ship" like method to construct a yolk-shell Z-scheme photocatalyst and to consume the photogenerated electrons of Ag_3PO_4 with the holes generated by MIL-53(Fe), for the boost of photocatalytic activity and restrain the photocorrosion of Ag_3PO_4. Besides, it was reported that there would be little amount of H_2O_2 generated during the photoreaction process of Ag_3PO_4 ($O_2 + 2H^+ + 2e^- \rightarrow H_2O_2$ (0.68 V vs NHE)), which would consume the photogenerated holes of Ag_3PO_4 ($H_2O_2 + 2\,h^+(Ag_3PO_4) \rightarrow O_2 + 2H^+$), and are adverse to the photocatalytic activity [44,45]. Accordingly, the photogenerated H_2O_2 from Ag_3PO_4 could be utilized by materials with Fe^{3+} through Fenton reaction [46]. Hence, it is assumed that combining Ag_3PO_4 with MIL-53(Fe) could take advantage of this H_2O_2 through a photo-Fenton-like reaction, further improved the photocatalytic performance of this composite. There is no such article available on the preparation of yolk-shell Ag_3PO_4@MIL-53(Fe) hybrid photocatalyst for the adsorption and removal of TC.

The present work aims to examine the feasibility of yolk-shell Ag_3PO_4@MIL-53(Fe) hybrids for enhancing TC removal. Firstly, the effect of Ag_3PO_4 dosage on TC removal was investigated under different TC concentrations. Quenching experiments and electron spin resonance (ESR) tests were then used to identify the dominant reactive species in this system. Besides, the concentration determination of H_2O_2 in the photoreaction was further tested. Photocatalytic stability of Ag_3PO_4 and Ag_3PO_4@MIL-53(Fe) was evaluated after five cycles. At last, we proposed the possible mechanism of Ag_3PO_4@MIL-53(Fe) hybrids in detail.

2. Experimental

This section was depicted in the Supplementary information (SI).

3. Results and discussions

By controlling the amount of Ag_3PO_4, Ag_3PO_4@MIL-53(Fe) composites with different mass ratio (MIL-53(Fe):Ag_3PO_4 = 5:1, 10:1, 20:1, 50:1, 100:1) were denoted as M:A = 5:1, M:A = 10:1. M:A = 20:1, M:A = 50:1, and M:A = 100:1. In this section, M:A = 5:1, M:A = 10:1, M:A = 20:1, MIL-53(Fe) samples were characterized by X-ray diffraction (XRD) to investigate their crystallographic structure. As depicted in Fig. 1A, the diffraction peaks of bare MIL-53(Fe) (marked with ★) were sharp and clear, indicating it possesses high crystallinity. All the diffraction peaks of bare MIL-53(Fe) sample were in agreement with the previous reports [47,48]. Four distinct diffraction peaks of Ag_3PO_4 (marked with ☆) at 33.3°, 47.8°, 55.0°, and 57.3° could be detected in the Ag_3PO_4@MIL-53(Fe) samples, which were related to the (2 1 0), (3 1 0), (3 2 0) and (3 2 1) planes of Ag_3PO_4 [49]. All modified samples displayed the characteristic peaks of Ag_3PO_4 and MIL-53(Fe), and no peaks related to other material were detected, suggesting the successful formation of Ag_3PO_4@MIL-53(Fe) samples. When the proportion of Ag_3PO_4 increased, the diffraction peaks intensities at $2\theta = 12.5°$ and 18.5° of MIL-53(Fe) decreased, which indicated that the bring in of Ag_3PO_4 particles in the MIL-53(Fe) synthesis procedure may restrain some planes of MIL-53(Fe) growth. Moreover, no observation of characteristic peak position of MIL-53(Fe) shifting in the Ag_3PO_4@MIL-53(Fe) sample, suggesting that the crystal structure was not destroyed by the introduction of Ag_3PO_4 in the synthesis progress.

The detailed molecular structure and functional groups information were characterized by Fourier transformed infrared spectra (FT-IR). As illustrated in Fig. 1B, the absorption peaks located at 1690, 1567, 1386, 750, and 545 cm^{-1} could be detected in the spectrum of MIL-53(Fe) sample. The absorption peak at 1690 cm^{-1} was corresponded to C=O stretching mode [50]. Peaks at 1567 and 1386 cm^{-1} were assigned to symmetric and asymmetric vibrations of carboxyl groups, respectively [51]. The peak at 750 cm^{-1} results from the C—H bonding vibrations in the benzene rings, while the peak at 545 cm^{-1} could be ascribed to the stretching vibration of F—O bond [52–54]. For bare Ag_3PO_4, two peaks located at 1072 and 550 cm^{-1} were presented, which could be allocated to the P—O stretching vibration of PO_4^{3-} and O=P—O flexural vibrations, respectively [55]. For M:A = 10:1 sample, the peak located at 1386 cm^{-1} was not observed, indicating that the symmetric vibrations of carboxyl groups may be destroyed by the introduction of Ag_3PO_4 during the synthesis process. Other characteristic peaks of MIL-53(Fe) and Ag_3PO_4 were clearly displayed in the spectrum of M:A = 10:1 sample, indicating the successful synthesis of Ag_3PO_4@MIL-53(Fe) composite.

X-ray photoelectron spectra (XPS) technique was used to characterize M:A = 10:1 sample to further obtain information about chemical states and surface composition. As depicted in the survey spectra (Fig. 2A), peaks corresponding to Fe, O, Ag, C, and P elements were presented, which was in agreement with the composite of M:A = 10:1. In the C 1s XPS spectrum (Fig. 2B), the peak located at 284.8 eV was belonging to the benzoic rings, and the peak at 288.6 eV could be assigned to the carboxylate groups of

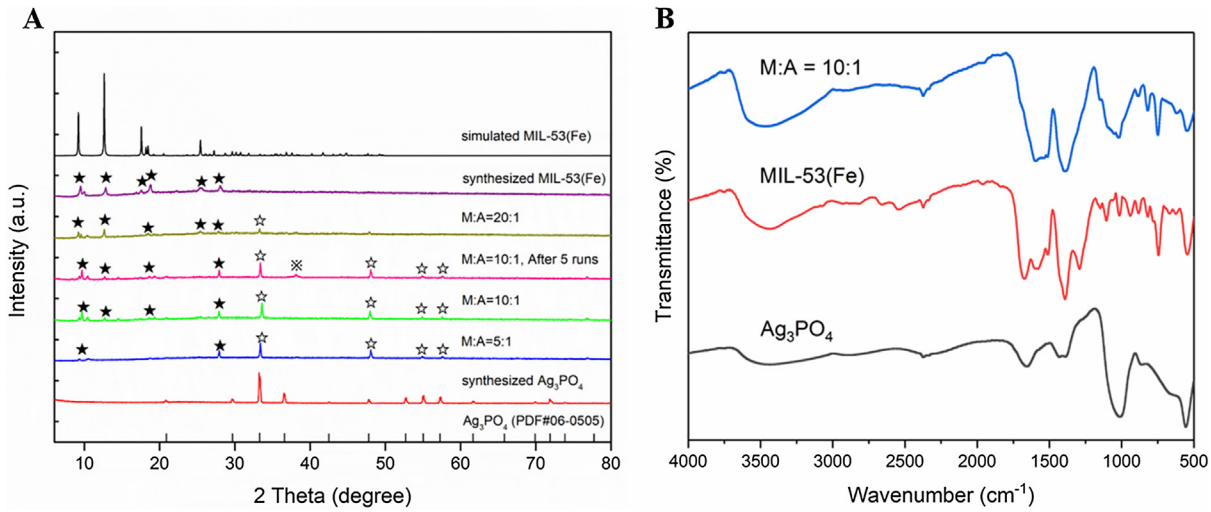

Fig. 1. A. XRD patterns of as-prepared samples and B. FT-IR spectra of M:A = 10:1, MIL-53(Fe), and Ag_3PO_4.

H_2BDC [56]. In the Fe 2p (Fig. 2C) spectrum, two peaks centered at 712.3 eV and 726.0 eV could be corresponded to Fe $2p_{3/2}$ and Fe $2p_{1/2}$, respectively, which confirmed the existence of Fe^{3+} in the M:A = 10:1 composite [57]. For the O 1s XPS spectrum (Fig. 2D), the peak located at 532.0 eV could be allocated to the O elements of H_2BDC, while the peak located at 531.2 eV was belonging to the O elements from Fe—O bonds or Ag_3PO_4 crystal [58–60]. As for the Ag 3d spectrum (Fig. 2E), the peaks located at 368.1 eV and 374.2 eV could be corresponded to Ag $3d_{5/2}$ and Ag $3d_{3/2}$, respectively [61]. This confirmed the existence of Ag^+ in M:A = 10:1 composite, while the P 2p spectrum (Fig. 2F) located at 133.6 eV demonstrated the existence of P^{5+} in M:A = 10:1 composite [62].

To analyze the morphology and size of as-prepared samples, scanning electron microscopy (SEM) and transmission electron microscopy (TEM) characterization methods were carried out. As shown in Fig. 3A and 3B, MIL-53(Fe) exhibited a nanorod morphology, with the average width and average length being 4–5 and 11–12 μm, respectively. After the introduction of Ag_3PO_4 (Fig. 3C and D), the morphology of M:A = 10:1 sample was barely changed, except that the average width of this sample was amplified to 5–6 μm. The yolk-shell structure of the as-prepared sample could be illustrated by the TEM images. It can be seen from Fig. 4 that black Ag_3PO_4 cores were randomly located, and were covered by the MIL-53(Fe) shell. This structure was conducive to the improvement of stability of Ag_3PO_4, and well protected the Ag_3PO_4 core from dissolution. The d spacing value of the lattice fringe, 0.268 nm, was clearly observed in Fig. 4D, which corresponded to the (2 1 0) crystallographic plane of Ag_3PO_4. In addition, the result of energy-dispersive X-ray spectroscopy (EDS) as shown in Fig. 3F further confirmed the existence of Ag, Fe and P elements in M:A = 10:1 sample. The weight percentage of Ag was 8.75 wt% in this composite, which demonstrated that the speculated amount of Ag_3PO_4 was introduced into the composite.

The nitrogen sorption analysis was used to measure the specific surface area and pore characteristic of M:A = 10:1 sample. As shown in Fig. 5A, M:A = 10:1 sample showed a type Ⅳ isothermal with a type H_3 hysteresis loop, which demonstrated that a mesopores material was successfully prepared. The Brunauer-Emmett-Teller (BET) surface area of M:A = 10:1 was calculated to be ca. 397.945 m^2/g, which was 11.75 times larger than that of MIL-53 (Fe) (ca. 33.866 m^2/g). Such expansion of BET surface area could be attributed to the increase in total pore volume by the introduction of Ag_3PO_4. According to the nitrogen sorption analysis, the total pore volume of MIL-53(Fe) was 0.024 cm^3/g, while the total pore volume of M:A = 10:1 sample was 0.341 cm^3/g. In addition, the pore size distribution figure (inset in Fig. 5A) shows that a number of pores less than 20 nm are generated, which further supports our speculation. High specific surface area usually means high adsorption amount and more surface active sites. Thus it is reasonable to deduce that M:A = 10:1 sample possesses better photocatalytic performance than bare MIL-53(Fe). In addition, the pore size distribution of samples and pore volume data was depicted in Table 1.

UV-vis diffuse reflectance spectra (UV-vis DRS) was applied to evaluate the absorption properties and the optical bandgap of catalysts. As shown in Fig. 5B, all the three samples revealed good absorption in the visible light range (<500 nm). After the introduction of Ag_3PO_4, the absorption range of M:A = 10:1 was expanded, which was beneficial to the improvement of photocatalytic activity. Besides, the bandgap edge (E_g) of semiconductors was calculated by the Kubelka-Munk Eq. (1) [63]:

$$\alpha h\nu = A(h\nu - E_g)^{n/2} \quad (1)$$

where α represents the absorption coefficient, ν represents the light frequency, E_g represents the bandgap energy, A is a constant, and n depends on the characteristics of the transition in a semiconductor. MIL-53(Fe) is a direct band semiconductor, while Ag_3PO_4 is an indirect transition semiconductor. As presented in Fig. 5C and 5D, the optical bandgap of MIL-53(Fe) and Ag_3PO_4 was measured as 1.78 eV and 2.35 eV, respectively.

The photocatalytic performance of the samples was assessed by the removal of TC antibiotics. Fig. 6A represents the decomposition rate of TC by different photocatalysts. In blank experiment (no photocatalysts were added), the TC concentration was barely changed, suggesting that the self-photolysis effect of TC could be ignored. After the introduction of Ag_3PO_4, the photocatalytic degradation rate was greatly enhanced, which was in the order of MIL-53(Fe) < M:A = 100:1 < M:A = 50:1 < M:A = 20:1 < M:A = 5:1 < M:A = 10:1. The pure MIL-53(Fe) showed the lowest TC removal efficiency (ca. 25.53%) with 1 h visible light irradiation, and M:A = 10:1 sample showed the highest TC removal efficiency (ca. 76.22%) under the same condition, which is 2.98 times than that of pure MIL-53(Fe), and better than that of BiOI [17], g-C_3N_4 [64,65], WO_3 [66], $BiVO_4$ [67,68], CdS [69], and ZnO [70] for the degradation of TC. According to the Langmuir-Hinshelwood kinetic model, we hypothesized that all the reactions followed the pseudo-first-order model (2):

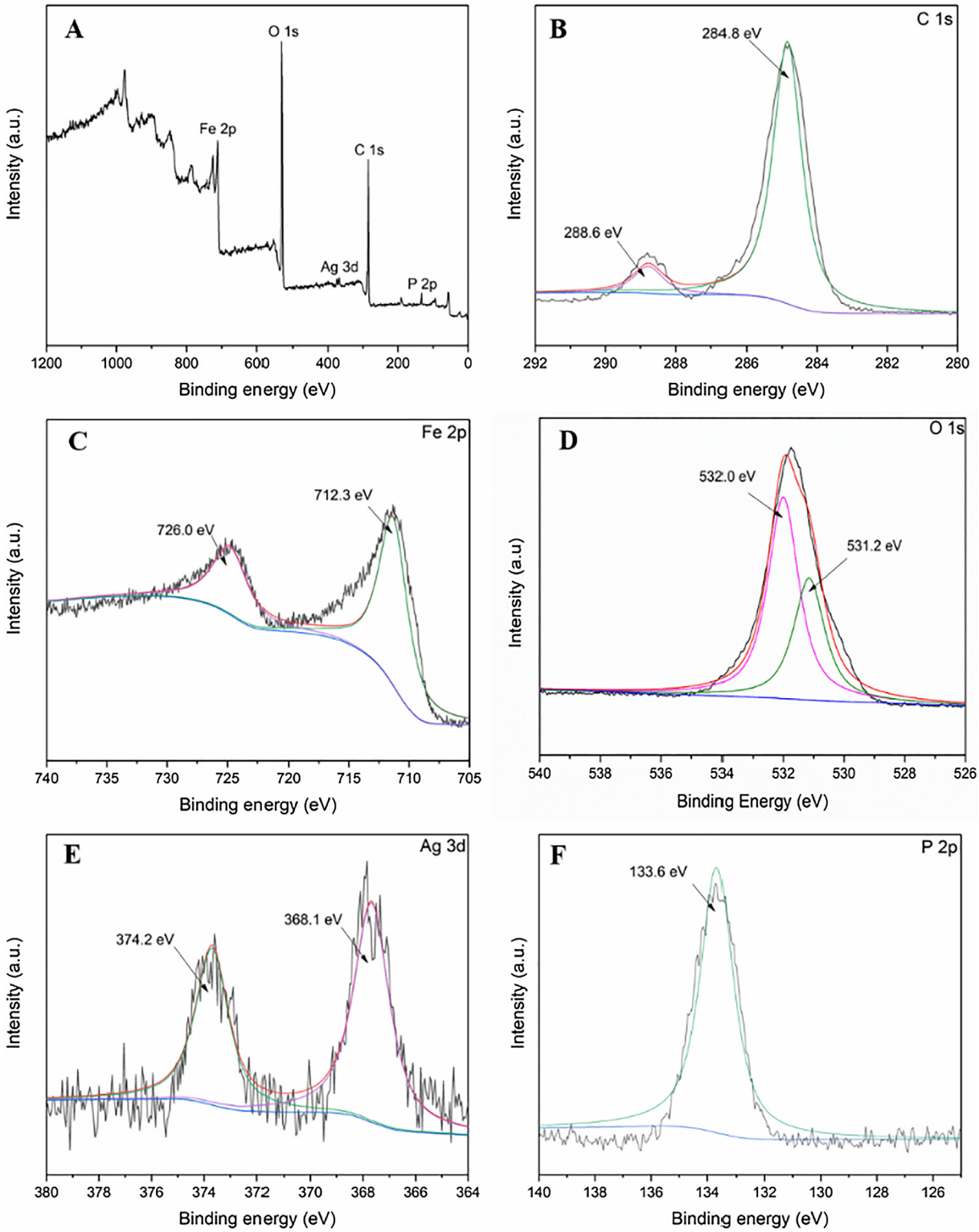

Fig. 2. The XPS spectra of M:A = 10:1: A. survey spectra, B. C 1s, C. Fe 2p, D. O 1s, E. Ag 3d, and F. P 2p.

$$\ln(C_0/C_t) = kt \times 100\% \quad (2)$$

where k behalf of the apparent reaction rate, C_0 and C_t presents the TC concentration at beginning and reaction time t, respectively. The k value of MIL-53(Fe), M:A = 100:1, M:A = 50:1, M:A = 20:1, M:A = 10:1, and M:A = 50:1 were 0.00219, 0.00184, 0.00359, 0.00441, 0.01232, and 0.01019 min^{-1}, respectively. Accordingly, the k value of M:A = 10:1 was 5.63 times larger than that of MIL-53(Fe), suggesting that the M:A = 10:1 possess the highest photocatalytic removal efficiency of TC in these samples. The improved photocatalytic activity can be ascribed to improved migration efficiency of photoinduced carriers. Upon visible light irradiation, the photoinduced electrons in the CB of Ag_3PO_4 could be consumed by the photoinduced holes in the VB of MIL-53(Fe), and holes remained in the VB of Ag_3PO_4 would be used in the degradation

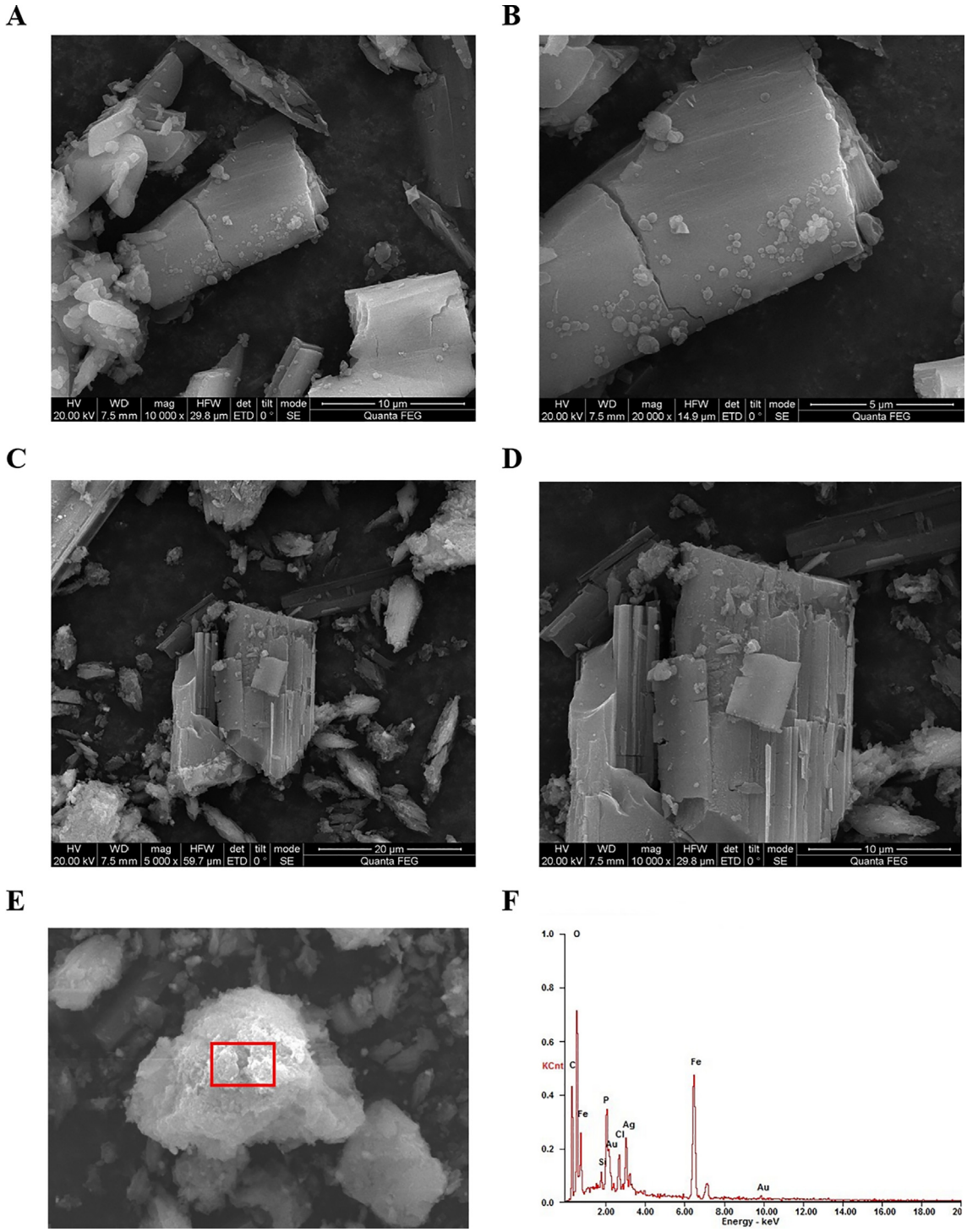

Fig. 3. A and B. SEM images of MIL-53(Fe); C, D and E. SEM images of M:A = 10:1; F. EDS image of M:A = 10:1.

of pollutants process. Besides, Fe^{3+} in MIL-53(Fe) would react with H_2O_2 (generated by Ag_3PO_4) to yield more reactive species to decompose organic pollutants. Moreover, adsorption-desorption equilibrium between TC and catalysts was improved by the introduction of Ag_3PO_4, which was consistent with the BET surface area results.

Fig. 6B exhibits the TC removal efficiency with different initial concentration of TC using M:A = 10:1 sample as photocatalyst, which decreased from 95.18% to 54.61% with the original TC concentration increasing from 10 to 50 mg/L. Generally, higher initial concentration possesses lower light permeability, which is bad for the absorption of photons. In addition, intermediates generated from the photocatalysis process would show a competitive behavior for the limited adsorption and catalytic sites compared to TC, which is bad for the removal of TC [71]. Thus, the removal rate at high initial TC concentration is much lower than that at low initial TC concentration. Furthermore, it is worth mentioning that due to the high adsorption amount at 10 mg/L (ca. 70.37%), 20 mg/L initial TC concentration was selected as the baseline in this experiment.

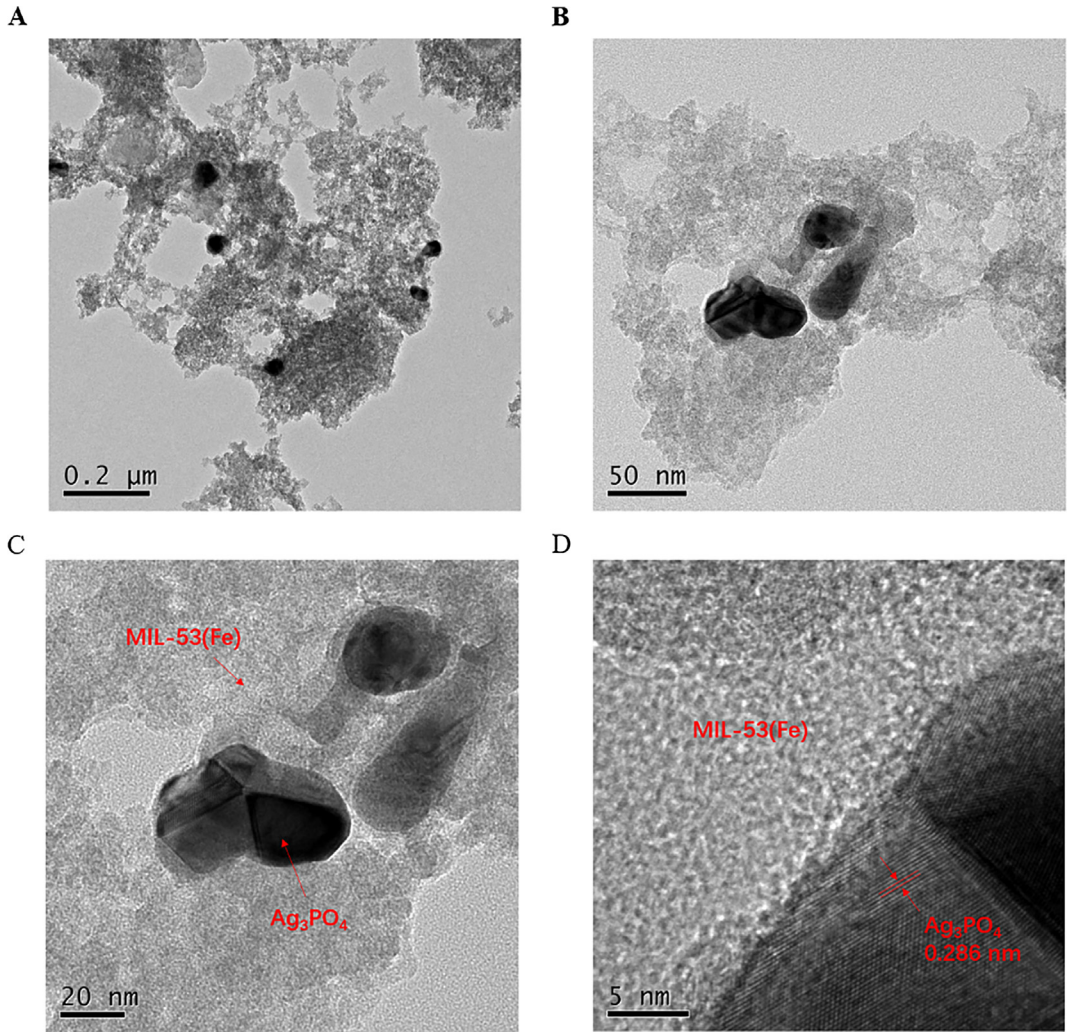

Fig. 4. TEM images of M:A = 10:1.

The photostability is of great importance to the practical applications. Fig. 6C shows the five time cycling experiment by using Ag_3PO_4 and M:A = 10:1 as catalysts. It can be seen that the removal efficiency of bare Ag_3PO_4 for TC was greatly degraded from 78.67% to 34.46% after five time run. However, only 6.09% losses at the three runs were detected in the M:A = 10:1 sample (from 76.22% to 70.13%), and remain 55.84% after five runs. This is manifested that the MOF shell play a vital role to protect the Ag_3PO_4 core from photocorrosion. The XRD pattern of M:A = 10:1 sample after five runs (Fig. 1A) shows almost the same pattern that the original M:A = 10:1 sample, while the peak at 38.1° could ascribed to the Ag^0 (marked with) particles that produced from photocorrosion of Ag_3PO_4. This characterization results also proved that this hybrid has a stable structure.

Photoluminescence (PL) spectra was applied to reveal the separation efficiency of photogenerated carriers in photocatalysts [71,72]. Fig. 7A shows the PL spectra of pure MIL-53(Fe), Ag_3PO_4, and M:A = 10:1 samples (excitation wavelength: 437 nm). The PL intensities were shown as follows: MIL-53(Fe) > Ag_3PO_4 > M:A = 10:1. In general, the higher PL signal, the lower separation efficiency of photogenerated carriers. Thus, both bare MIL-53(Fe) and Ag_3PO_4 presented a relatively high recombination rate of photogenerated carriers, and M:A = 10:1 sample possesses the lowest recombination rate among these three photocatalysts. This agrees well with the result of TC degradation experiment. The PL results indicated that the import of Ag_3PO_4 into MIL-53(Fe) could effectively promote the separation efficiency of photoinduced carriers, thus enhancing the photocatalytic activity. The highest intensity could be attributed to the efficient charge transfer and separation process, which are contributed to the yolk-shell heterostructure between Ag_3PO_4 and MIL-53(Fe).

Photocurrent response and electrochemical impedance spectra (EIS) was used for further investigation of charge separation and migration behavior of catalysts. As presented in Fig. 7B, photocurrent intensity of pure MIL-53(Fe) was barely observed, while pure Ag_3PO_4 showed relatively lower photocurrent intensity contrast to M:A = 10:1 sample. In fact, photocurrent intensity of M:A = 10:1 was about 1.53 times and 9.2 times higher than that of Ag_3PO_4 and MIL-53(Fe), respectively. As depicted in Fig. 7C, the semicircular diameter of these tested samples was in the sequence of MIL-53 (Fe) > Ag_3PO_4 > M:A = 10:1. Normally, a smaller arc radius of the Nyquist plots in EIS test means a smaller charge transfer resistance (or a higher efficiency in charge transfer) [73]. Hence, M:A = 10:1 sample showed the highest efficiency in charge transfer among these three samples, which were in consistent with the above-discussed results.

To evidence the H_2O_2 generated by Ag_3PO_4 could be decomposed by the introduction of MIL-53(Fe), a permanganate titration was used to detect the concentration of H_2O_2 for M:A = 10:1 and Ag_3PO_4 upon visible light irradiation. As displayed in Fig. 7D, it

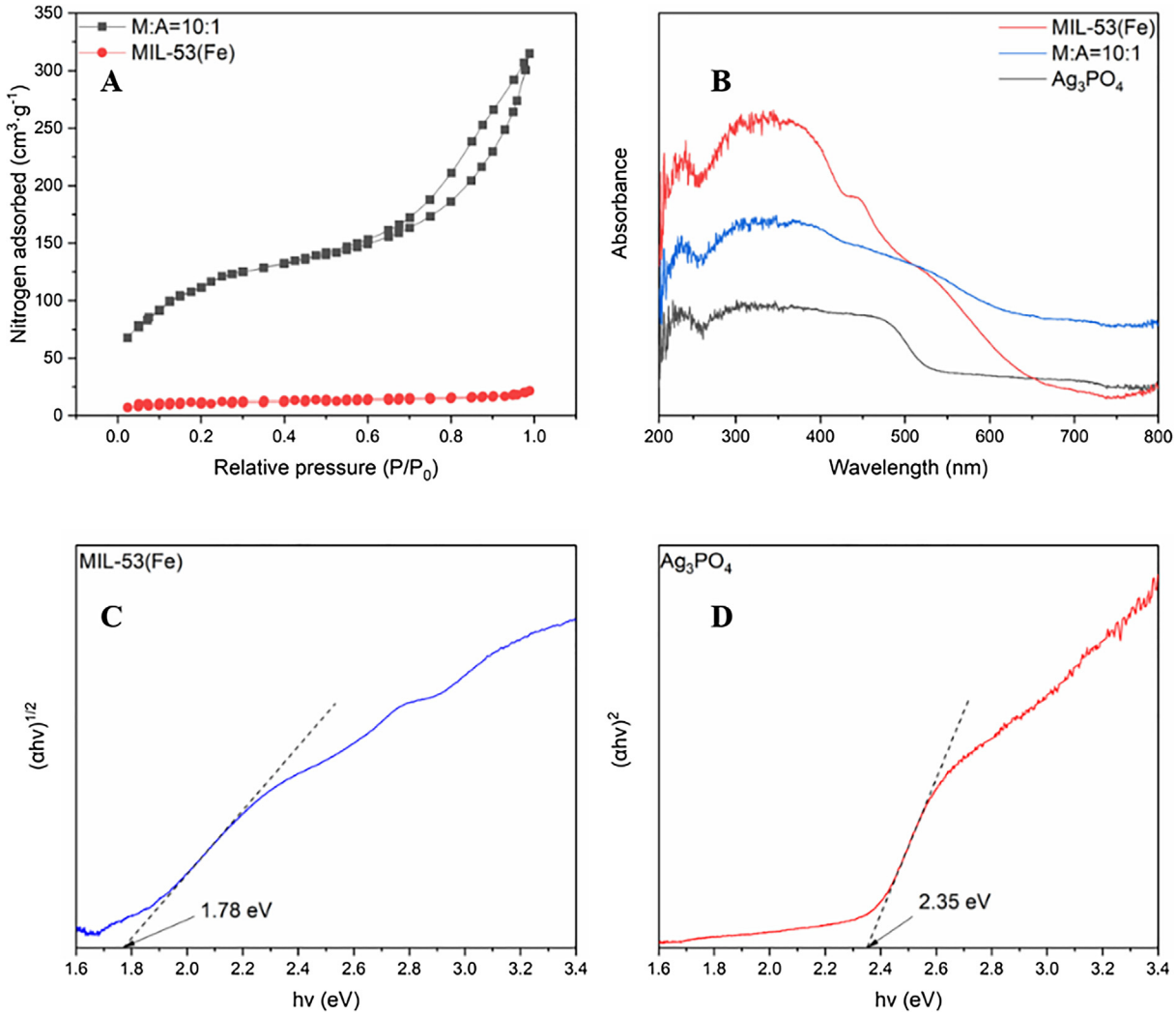

Fig 5. A. Nitrogen adsorption-desorption isotherm of the as-prepared MIL-53(Fe) and M:A = 10:1, inset shows the pore size distribution curves; B. UV-vis DRS spectra of MIL-53(Fe), Ag_3PO_4, and M:A = 10:1 sample; C. band gap energy of MIL-53(Fe); and D. band gap energy of Ag_3PO_4.

Table 1
Surface area, pore size, and pore volume data for MIL-53(Fe) and M:A = 10:1.

Samples	Surface area (m^2/g)	Pore size (nm)	V_t (cm^3/g)
MIL-53(Fe)	33.866	3.919	0.024
M:A = 10:1	397.945	4.896	0.341

Note: the pore size distribution of samples were calculated by Barrett-Joyner-Halenda method; and V_t (total pore volume) were determined at P/P0 = 0.99.

can be clearly observed that for pure Ag_3PO_4, the concentration of H_2O_2 could reach to 154 μmol/L, while for M:A = 10:1 sample, the detected H_2O_2 concentration is 52 μmol/L. This results indicated that a big part of generated H_2O_2 on the Ag_3PO_4 core would be quickly decomposed by the MIL-53(Fe) shell, which reduces the consumption of holes (from Ag_3PO_4) as well as generates more reactive species (through photo-Fenton-like reaction) to react with target pollutants.

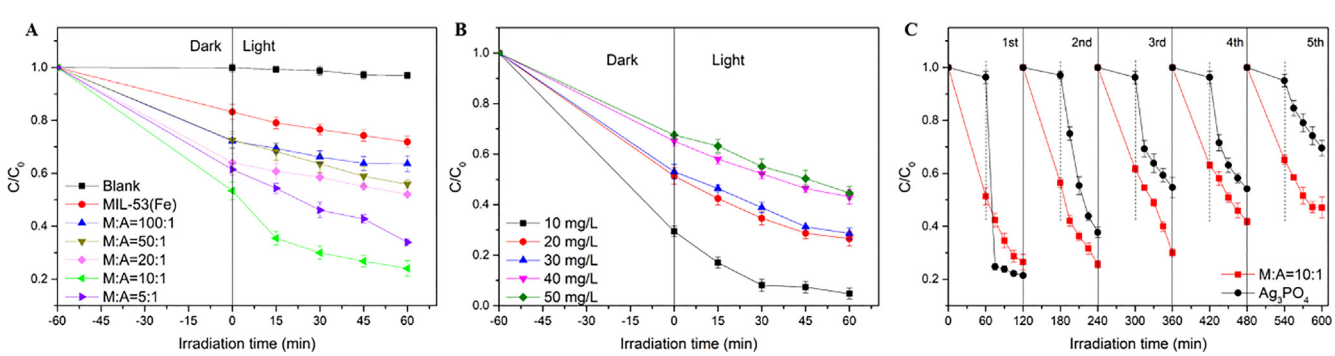

Fig. 6. A. photocatalytic degradation of 20 mg/L TC by different samples; B. effects of the initial concentration of TC on the photocatalytic activities of M:A = 10:1 sample; C. cycling photocatalytic tests of M:A = 10:1 and Ag_3PO_4 for degradation of 20 mg/L TC.

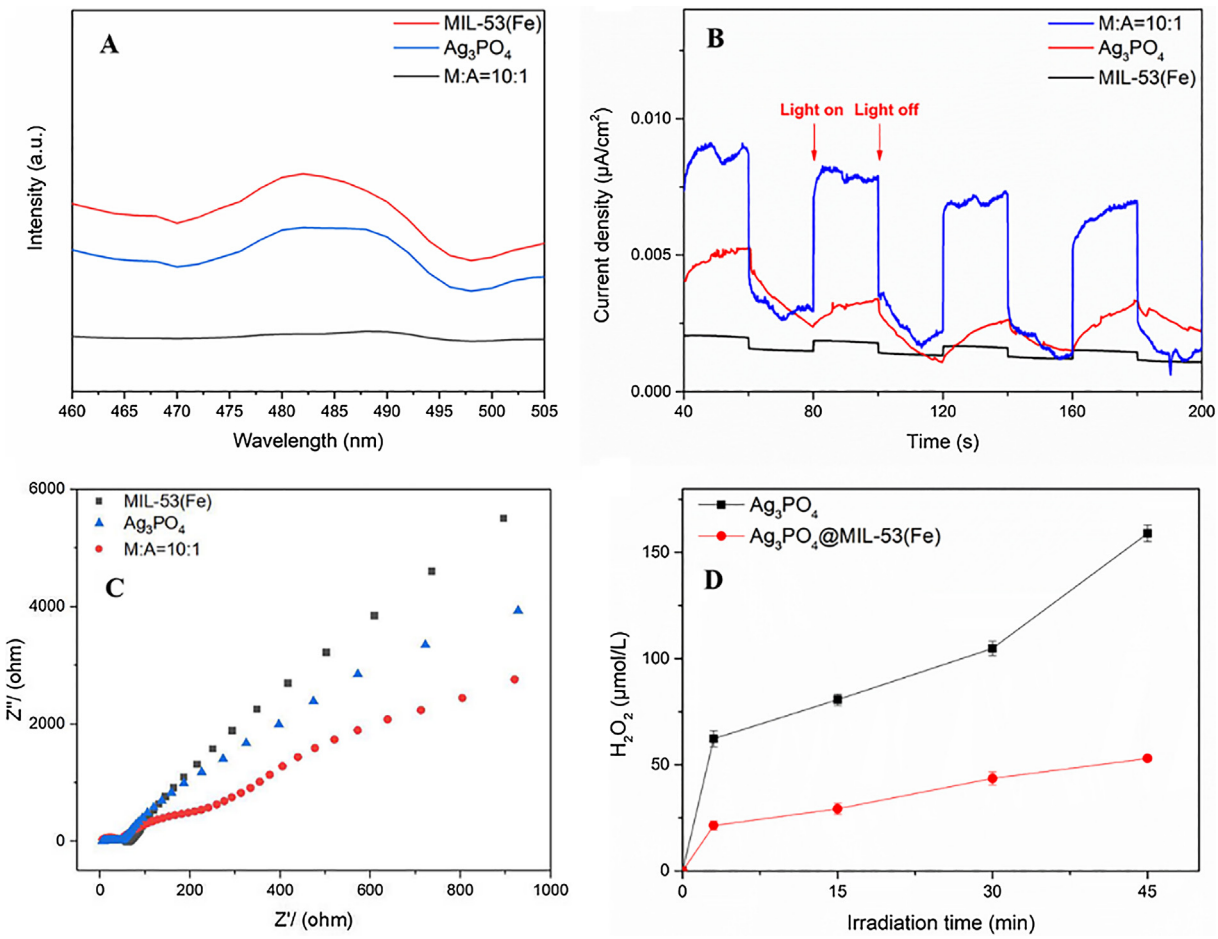

Fig. 7. A. PL spectra, B. photocurrent responses, and C. EIS spectra of MIL-53(Fe), Ag_3PO_4, and M:A = 10:1; D·H_2O_2 concentration detection of M:A = 10:1 and Ag_3PO_4 under visible light irradiation.

The introduction of Ag_3PO_4 as a core into the MIL-53(Fe) shell could effectively suppress the recombination of photoinduced electron-hole pairs. To explore the dominant reactive species in this reaction, three types of chemicals, BQ, $Na_2C_2O_4$ and IPA were used to trap $\cdot O_2^-$ radicals, h^+ radicals, and ·OH radicals, respectively [47,74,75]. As depicted in Fig. 8A, when $Na_2C_2O_4$ and BQ were added in this system, the degradation rate decreased from 76.22% to 48.34% and 53.32%, respectively. The addition of IPA also had an influence on the removal efficiency of TC, but only 10.14% of reduction was measured. The above results suggested that the h^+ and $\cdot O_2^-$ were the predominant reactive species for the TC removal by M:A = 10:1 samples.

To further confirm the trapping experiment results, the electron spin resonance (ESR) technique was carried out. DMPO was used to capture the $\cdot O_2^-$ and ·OH radicals, while TEMPO was used to capture the h^+ radicals. As displayed in Fig. 8B and 8C, no signals in dark condition were observed in both ESR spectra, whereas four characteristic peaks of DMPO-$\cdot O_2^-$ and DMPO-·OH were detected after the light turns on. As the irradiation time increases, the peak intensity also increased. This demonstrated the existence of $\cdot O_2^-$ and ·OH radicals in this system. Furthermore, as presented in Fig. 8D, three strong characteristic peaks of TEMPO-h^+ were detected in both dark and visible light condition. In addition, the peak intensity increased with the irradiation time goes on, which verified that the h^+ radicals also worked in this system.

In general, the high photocatalytic performance of yolk-shell Ag_3PO_4@MIL-53(Fe) catalyst could be attributed to the high surface area, absorption capability and separation efficiency of photoinduced charge carriers. Based on the above-experimental results, the possible photocatalytic mechanism in Ag_3PO_4@MIL-53(Fe) yolk-shell structure composites was depicted in Fig. 9. Ag_3PO_4 particles were randomly located in the cavities of MIL-53(Fe) shell. As long as visible light irradiation started, both Ag_3PO_4 and MIL-53 (Fe) could be activated to yield electrons and holes, and the photoinduced electrons in the CB of Ag_3PO_4 could be depleted by the photoinduced h^+ in the VB of MIL-53(Fe). Hence, the separation efficiency increased. Holes remained in the VB of Ag_3PO_4 could take part in the degradation of pollutants process. Besides, a small part of the remained electrons in the CB of Ag_3PO_4 could be transferred into H_2O_2, which may restrain the photocatalytic activity of Ag_3PO_4 ($H_2O_2 + 2\,h^+(Ag_3PO_4) \rightarrow O_2 + 2H^+$). Thus, when the Ag_3PO_4 cores were covered by MIL-53(Fe) shell, the generated H_2O_2 could be consumed via a photo-Fenton-like reaction:

$$\text{MIL-53(Fe)} + h\nu \rightarrow e^- + h^+ \tag{3}$$

$$Fe^{3+} + e^-(\text{MIL-53(Fe)}) \rightarrow Fe^{2+} \tag{4}$$

$$Fe(OH)^{2+} + h\nu \rightarrow Fe^{2+} + \cdot OH \tag{5}$$

$$Fe^{2+} + H_2O_2 \rightarrow Fe^{2+} + \cdot OH + OH^- \tag{6}$$

$$Fe^{3+} + H_2O_2 \rightarrow \cdot OOH + H^+ \tag{7}$$

In addition, the stability of Ag_3PO_4 could be increased by the protection shell of MIL-53(Fe), which makes a big step forward for its practice application.

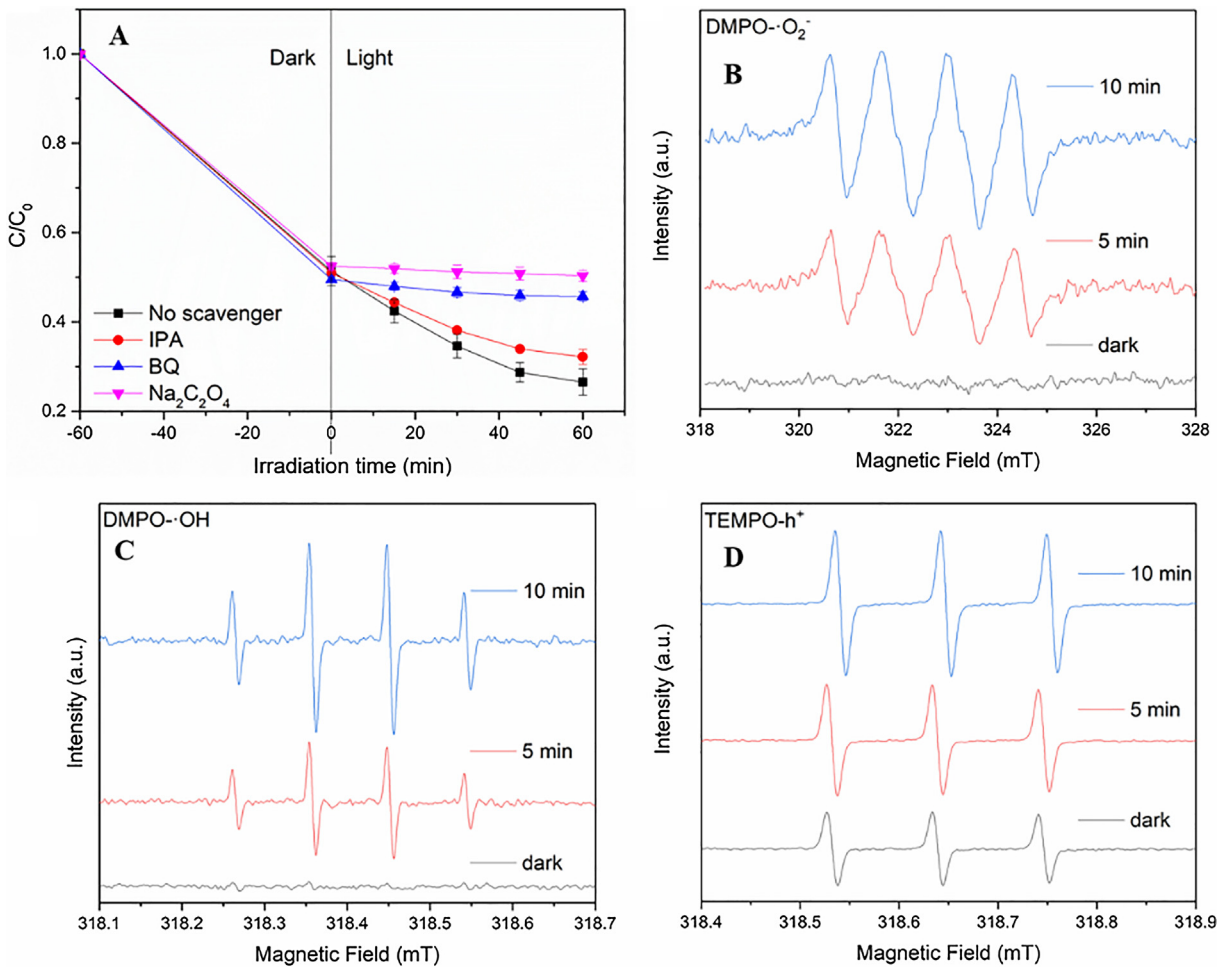

Fig. 8. A. photocatalytic curves of M:A = 10:1 sample with different scavengers for the degradation of TC; B. Spin-trapping ESR spectra for M:A = 10:1 in methanol dispersion for DMPO-$^{\cdot}O_2^-$; C. in aqueous dispersion for DMPO-·OH; and D. in aqueous dispersion for TEMPO-h^+ under both dark and visible light irradiation.

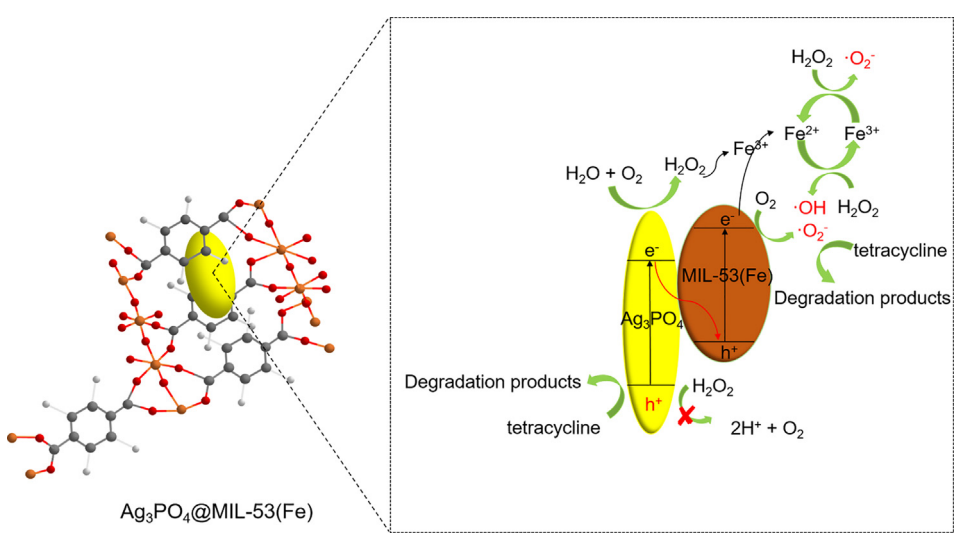

Fig. 9. Proposed photocatalytic mechanism in Ag_3PO_4@MIL-53(Fe) yolk-shell structure composites.

4. Conclusions

In this work, we successfully synthesized a yolk-shell Ag_3PO_4@-MIL-53(Fe) Z-scheme photocatalyst via a "bottle-around-ship" like method, which exhibited enlarged BET surface area and superior photocatalytic performance for TC removal upon visible light irradiation. The increased BET surface area is attributed to the introduction of Ag_3PO_4 makes the porosity of hybrids greatly improved. The total pore volume of MIL-53(Fe) is 0.024 cm^3/g, while after the introduction of Ag_3PO_4 cores, the total pore volume

was enlarged to 0.341 cm^3/g, both the BET surface area and total pore volume are far more than the Ag_3PO_4/MIL-53(Fe) composite that Xie et al. reported [39]. As is well-known, high specific surface area usually means high adsorption amount and more surface active sites, which is conducive to improve the photocatalytic performance. In addition, the boosted photocatalytic performance was mainly ascribed to the Z-scheme structure which consumed the photogenerated $e^-(Ag_3PO_4)$ and h^+(MIL-53(Fe)), leading to more $h^+(Ag_3PO_4)$ and e^- (MIL-53(Fe)) participate in the photocatalytic procedure. Moreover, this hybrid composites subtly took advantage of MIL-53(Fe) for a photo-Fenton-like reaction to decompose the unwanted H_2O_2 (generated by Ag_3PO_4), which not only restrained the meaningless consumption of $h^+(Ag_3PO_4)$, but also generated more reactive species (h^+ and ·OH) to take part in the photocatalytic reaction. Besides, the yolk-shell structure was conducive to inhibit the dissolution of Ag_3PO_4, thereby improving its stability. This study offers a simple way to design and fabricate yolk-shell structure photocatalysts with large surface area and excellent photocatalytic performance for environmental remediation.

Declaration of Competing Interest

None.

Acknowledgements

The study is financially supported by the Program for the National Natural Science Foundation of China (51521006, 51508178, 51779089, 51709101, and 51508177), the Three Gorges Follow-up Research Project (2017HXXY-05), and the Program for Changjiang Scholars and Innovative Research Team in University (IRT-13R17).

References

[1] J.-L. Gong, B. Wang, G.-M. Zeng, C.-P. Yang, C.-G. Niu, Q.-Y. Niu, W.-J. Zhou, Y. Liang, Removal of cationic dyes from aqueous solution using magnetic multi-wall carbon nanotube nanocomposite as adsorbent, J. Hazard. Mater. 164 (2) (2009) 1517–1522.
[2] P. Xu, G.M. Zeng, D.L. Huang, C.L. Feng, S. Hu, M.H. Zhao, C. Lai, Z. Wei, C. Huang, G.X. Xie, Z.F. Liu, Use of iron oxide nanomaterials in wastewater treatment: a review, Sci. Total Environ. 424 (2012) 1–10.
[3] K. He, G. Chen, G. Zeng, A. Chen, Z. Huang, J. Shi, T. Huang, M. Peng, L. Hu, Three-dimensional graphene supported catalysts for organic dyes degradation, Appl. Catal. B 228 (2018) 19–28.
[4] Y. Wang, Y. Zhu, Y. Hu, G. Zeng, Y. Zhang, C. Zhang, C. Feng, How to construct DNA hydrogels for environmental applications: advanced water treatment and environmental analysis, Small 14 (17) (2018) 1703305.
[5] X. Tang, G. Zeng, C. Fan, M. Zhou, L. Tang, J. Zhu, J. Wan, D. Huang, M. Chen, P. Xu, C. Zhang, Y. Lu, W. Xiong, Chromosomal expression of CadR on Pseudomonas aeruginosa for the removal of Cd(II) from aqueous solutions, Sci. Total Environ. 636 (2018) 1355–1361.
[6] S. Ye, G. Zeng, H. Wu, C. Zhang, J. Liang, J. Dai, Z. Liu, W. Xiong, J. Wan, P. Xu, M. Cheng, Co-occurrence and interactions of pollutants, and their impacts on soil remediation—A review, Crit. Rev. Environ. Sci. Technol. 47 (2017) 1528–1553.
[7] L. Qin, G. Zeng, C. Lai, D. Huang, P. Xu, C. Zhang, M. Cheng, X. Liu, S. Liu, B. Li, H. Yi, "Gold rush" in modern science: fabrication strategies and typical advanced applications of gold nanoparticles in sensing, Coord. Chem. Rev. 359 (2018) 1–31.
[8] S. Ye, G. Zeng, H. Wu, C. Zhang, J. Dai, J. Liang, J. Yu, X. Ren, H. Yi, M. Cheng, C. Zhang, Biological technologies for the remediation of co-contaminated soil, Crit. Rev. Biotechnol. 37 (8) (2017) 1062–1076.
[9] B. Song, M. Chen, S. Ye, P. Xu, G. Zeng, J. Gong, J. Li, P. Zhang, W. Cao, Effects of multi-walled carbon nanotubes on metabolic function of the microbial community in riverine sediment contaminated with phenanthrene, Carbon 144 (2019) 1–7.
[10] H. Yi, M. Jiang, D. Huang, G. Zeng, C. Lai, L. Qin, C. Zhou, B. Li, X. Liu, M. Cheng, W. Xue, P. Xu, C. Zhang, Advanced photocatalytic Fenton-like process over biomimetic hemin-Bi2WO6 with enhanced pH, J. Taiwan Inst. Chem. Eng. 93 (2018) 184–192.
[11] S. Li, W. Shi, W. Liu, H. Li, W. Zhang, J. Hu, Y. Ke, W. Sun, J. Ni, A duodecennial national synthesis of antibiotics in China's major rivers and seas 2005–2016, Sci. Total Environ. 615 (2018) 906–917.
[12] Y. Deng, L. Tang, G. Zeng, J. Wang, Y. Zhou, J. Wang, J. Tang, L. Wang, C. Feng, Facile fabrication of mediator-free Z-scheme photocatalyst of phosphorous-doped ultrathin graphitic carbon nitride nanosheets and bismuth vanadate composites with enhanced tetracycline degradation under visible light, J. Coll. Interf. Sci. 509 (2017) 219.
[13] J.A. Park, A. Nam, J.H. Kim, S.T. Yun, J.W. Choi, S.H. Lee, Blend-electrospun graphene oxide/Poly(vinylidene fluoride) nanofibrous membranes with high flux, tetracycline removal and anti-fouling properties, Chemosphere 207 (2018) 347.
[14] X. Zhu, Y. Liu, F. Qian, C. Zhou, S. Zhang, J. Chen, Preparation of magnetic porous carbon from waste hydrochar by simultaneous activation and magnetization for tetracycline removal, Bioresour. Technol. 154 (2) (2014) 209–214.
[15] B. Kakavandi, A. Takdastan, N. Jaafarzadeh, M. Azizi, A. Mirzaei, A. Azari, Application of Fe3O4@C catalyzing heterogeneous UV-Fenton system for tetracycline removal with a focus on optimization by a response surface method, J. Photochem. Photobiol. A 314 (2016) 178–188.
[16] D. Wang, F. Jia, H. Wang, F. Chen, Y. Fang, W. Dong, G. Zeng, X. Li, Q. Yang, X. Yuan, efficient adsorption and photocatalytic degradation of tetracycline by Fe-based MOFs, J. Coll. Interf. Sci. 519 (2018) 273.
[17] Y. Yang, Z. Zeng, Z. Chen, D. Huang, G. Zeng, X. Rong, L. Cui, C. Zhou, G. Hai, W. Xue, Construction of iodine vacancy-rich BiOI/Ag@AgI Z-scheme heterojunction photocatalysts for visible-light-driven tetracycline degradation: transformation pathways and mechanism insight, Chem. Eng. J. (2018). S1385894718309069.
[18] C. Zhou, C. Lai, P. Xu, G. Zeng, D. Huang, Z. Li, C. Zhang, M. Cheng, L. Hu, J. Wan, Rational design of carbon-doped carbon nitride/Bi12O17Cl2 composites: a promising candidate photocatalyst for boosting visible-light-driven photocatalytic degradation of tetracycline, Sustain. Chem. Eng. 6 (3) (2018) 4174–4184.
[19] L. Jiang, X. Yuan, G. Zeng, Z. Wu, J. Liang, X. Chen, L. Leng, H. Wang, H. Wang, Metal-free efficient photocatalyst for stable visible-light photocatalytic degradation of refractory pollutant, Appl. Catal. B 221 (2017) 715–725.
[20] W. Hou, X. Yuan, W. Yan, G. Zeng, H. Dong, X. Chen, L. Leng, Z. Wu, L. Peng, In situ synthesis of In_2S_3 @MIL-125(Ti) core–shell microparticle for the removal of tetracycline from wastewater by integrated adsorption and visible-light-driven photocatalysis, Appl. Catal. B 186 (2016) 19–29.
[21] Y. Yang, C. Zhang, C. Lai, G. Zeng, D. Huang, M. Cheng, J. Wang, F. Chen, C. Zhou, W. Xiong, BiOX (X = Cl, Br, I) photocatalytic nanomaterials: Applications for fuels and environmental management, Adv. Coll. Interf. Sci. (2018) 19–29.
[22] C. Zhou, C. Lai, C. Zhang, G. Zeng, D. Huang, M. Cheng, L. Hu, W. Xiong, M. Chen, J. Wang, Y. Yang, L. Jiang, Semiconductor/boron nitride composites: Synthesis, properties, and photocatalysis applications, Appl. Catal. B 238 (2018) 6–18.
[23] S. Ye, M. Yan, X. Tan, J. Liang, G. Zeng, H. Wu, B. Song, C. Zhou, Y. Yang, H. Wang, Facile assembled biochar-based nanocomposite with improved graphitization for efficient photocatalytic activity driven by visible light, Appl. Catal. B 250 (2019) 78–88.
[24] H. Yi, M. Yan, D. Huang, G. Zeng, C. Lai, M. Li, X. Huo, L. Qin, S. Liu, X. Liu, B. Li, H. Wang, M. Shen, Y. Fu, X. Guo, Synergistic effect of artificial enzyme and 2D nano-structured Bi_2WO_6 for eco-friendly and efficient biomimetic photocatalysis, Appl. Catal. B 250 (2019) 52–62.
[25] H. Wang, Z. Zeng, P. Xu, L. Li, G. Zeng, R. Xiao, Z. Tang, D. Huang, L. Tang, C. Lai, D. Jiang, Y. Liu, H. Yi, L. Qin, S. Ye, X. Ren, W. Tang, Recent progress in covalent organic framework thin films: fabrications, applications and perspectives, Chem. Soc. Rev. 48 (2) (2019) 488–516.
[26] D. Jiang, M. Chen, H. Wang, G. Zeng, D. Huang, M. Cheng, Y. Liu, W. Xue, Z. Wang, The application of different typological and structural MOFs-based materials for the dyes adsorption, Coord. Chem. Rev. 380 (2019) 471–483.
[27] B. Li, H.M. Wen, Y. Cui, W. Zhou, G. Qian, B. Chen, Emerging Multifunctional Metal-Organic Framework Materials, Adv. Mater. 28 (40) (2016) 8819–8860.
[28] E. Haque, J.W. Jun, S.H. Jhung, Adsorptive removal of methyl orange and methylene blue from aqueous solution with a metal-organic framework material, iron terephthalate (MOF-235), J. Hazard. Mater. 185 (1) (2011) 507–511.
[29] M. Anbia, V. Hoseini, S. Sheykhi, Sorption of methane, hydrogen and carbon dioxide on metal-organic framework, iron terephthalate (MOF-235), J. Ind. Eng. Chem. 18 (3) (2012) 1149–1152.
[30] W. Xiong, Z. Zeng, X. Li, G. Zeng, R. Xiao, Z. Yang, Y. Zhou, C. Zhang, M. Cheng, L. Hu, C. Zhou, L. Qin, R. Xu, Y. Zhang, Multi-walled carbon nanotube/amino-functionalized MIL-53(Fe) composites: remarkable adsorptive removal of antibiotics from aqueous solutions, Chemosphere 210 (2018) 1061–1069.
[31] W. Xiong, G. Zeng, Z. Yang, Y. Zhou, C. Zhang, M. Cheng, Y. Liu, L. Hu, J. Wan, C. Zhou, R. Xu, X. Li, Adsorption of tetracycline antibiotics from aqueous solutions on nanocomposite multi-walled carbon nanotube functionalized MIL-53(Fe) as new adsorbent, Sci. Total Environ. 627 (2018) 235–244.
[32] X. Li, P. Xu, M. Chen, G. Zeng, D. Wang, F. Chen, W. Tang, C. Chen, C. Zhang, X. Tan, Application of silver phosphate-based photocatalysts: Barriers and solutions, Chem. Eng. J. 366 (2019) 339–357.
[33] L. Zhang, J. Zhang, G. Zeng, H. Dong, Y. Chen, C. Huang, Y. Zhu, R. Xu, Y. Cheng, K. Hou, W. Cao, W. Fang, Multivariate relationships between microbial communities and environmental variables during co-composting of sewage sludge and agricultural waste in the presence of PVP-AgNPs, Bioresour. Technol. 261 (2018) 10–18.
[34] K. He, Z. Zeng, A. Chen, G. Zeng, R. Xiao, P. Xu, Z. Huang, J. Shi, L. Hu, G. Chen, Advancement of Ag–Graphene based nanocomposites: an overview of synthesis and its applications, Small 14 (32) (2018) 1800871.

[35] Z. Huang, K. He, Z. Song, G. Zeng, A. Chen, L. Yuan, H. Li, L. Hu, Z. Guo, G. Chen, Antioxidative response of Phanerochaete chrysosporium against silver nanoparticle-induced toxicity and its potential mechanism, Chemosphere 211 (2018) 573–583.

[36] G. Li, S. Zhao, Y. Zhang, Z. Tang, Metal-organic frameworks encapsulating active nanoparticles as emerging composites for catalysis: recent progress and perspectives, Adv. Mater. 30 (51) (2018) e1800702.

[37] S. Mosleh, M.R. Rahimi, M. Ghaedi, K. Dashtian, Sonophotocatalytic degradation of trypan blue and vesuvine dyes in the presence of blue light active photocatalyst of Ag3PO4/Bi2S3-HKUST-1-MOF: Central composite optimization and synergistic effect study, Ultrason. Sonochem. 32 (2016) 387–397.

[38] S. Mosleh, M.R. Rahimi, M. Ghaedi, K. Dashtian, S. Hajati, S. Wang, Ag3PO4/AgBr/Ag-HKUST-1-MOF composites as novel blue LED light active photocatalyst for enhanced degradation of ternary mixture of dyes in a rotating packed bed reactor, Chem. Eng. Process. Process Intensif. 114 (2017) 24–38.

[39] X.-Y. Xu, C. Chu, H. Fu, X.-D. Du, P. Wang, W. Zheng, C.-C. Wang, Light-responsive UiO-66-NH_2/Ag_3PO_4 MOF-nanoparticle composites for the capture and release of sulfamethoxazole, Chem. Eng. J. 350 (2018) 436–444.

[40] F.A. Sofi, K. Majid, O. Mehraj, The visible light driven copper based metal-organic-framework heterojunction:HKUST-1@Ag-Ag3PO4 for plasmon enhanced visible light photocatalysis, J. Alloy. Compd. 737 (2018) 798–808.

[41] T. Zhou, G. Zhang, H. Zhang, H. Yang, P. Ma, X. Li, X. Qiu, G. Liu, Highly efficient visible-light-driven photocatalytic degradation of rhodamine B by a novel Z-scheme Ag_3PO_4/MIL-101/$NiFe_2O_4$ composite, Catal. Sci. Technol. 8 (9) (2018) 2402–2416.

[42] X. Qian, H. Xu, X. Zhang, R. Lei, J. Gao, S. Xu, Enhanced visible-light-driven photocatalytic activity of Ag_3PO_4/metal–organic framework composite, Polyhedron 163 (2019) 1–6.

[43] R.A. Rather, Z.N. Siddiqui, Silver phosphate supported on metal–organic framework (Ag_3PO_4@MOF-5) as a novel heterogeneous catalyst for green synthesis of indenoquinolinediones, Appl. Organomet. Chem. (2019) e5176.

[44] H. Katsumata, M. Taniguchi, S. Kaneco, T. Suzuki, Photocatalytic degradation of bisphenol A by Ag_3PO_4 under visible light, Catal. Commun. 34 (13) (2013) 30–34.

[45] S. Huanga, Y. Xua, T. Zhoua, X. Meng, M. Yun, Q. Liua, L. Jinga, X. Hui, H. Lia, Constructing magnetic catalysts with in-suit solid-liquid interfacial photo-Fenton-like reaction over Ag_3PO_4 @$NiFe_2O_4$ composites, Appl. Catal. B 225 (2017).

[46] S. Huang, Y. Xu, T. Zhou, M. Xie, Y. Ma, Q. Liu, L. Jing, H. Xu, H. Li, Constructing magnetic catalysts with in-situ solid-liquid interfacial photo-Fenton-like reaction over Ag_3PO_4@$NiFe_2O_4$ composites, Appl. Catal. B 225 (2018) 40–50.

[47] L. Xie, Z. Yang, W. Xiong, Y. Zhou, J. Cao, Y. Peng, X. Li, C. Zhou, R. Xu, Y. Zhang, Construction of MIL-53(Fe) metal-organic framework modified by silver phosphate nanoparticles as a novel Z-scheme photocatalyst: Visible-light photocatalytic performance and mechanism investigation, Appl. Surf. Sci. 465 (2019) 103–115.

[48] F. Millange, N. Guillou, R.I. Walton, J.M. Grenèche, I. Margiolaki, G. Férey, Effect of the nature of the metal on the breathing steps in MOFs with dynamic frameworks, Chem. Commun. 39 (39) (2008) 4732–4734.

[49] Y. Zhiguo, Y. Jinhua, K. Naoki, K. Tetsuya, O. Shuxin, S.W. Hilary, Y. Hui, C. Junyu, L. Wenjun, L. Zhaosheng, An orthophosphate semiconductor with photooxidation properties under visible-light irradiation, Nat. Mater. 9 (7) (2010) 559–564.

[50] L. Ai, C. Zhang, L. Li, J. Jing, Iron terephthalate metal–organic framework: Revealing the effective activation of hydrogen peroxide for the degradation of organic dye under visible light irradiation, Appl. Catal. B 148–149 (1) (2014) 191–200.

[51] C. Zhang, L. Ai, J. Jing, Graphene hybridized photoactive iron terephthalate with enhanced photocatalytic activity for the degradation of Rhodamine B under visible light, Ind. Eng. Chem. Res. 54 (1) (2015) 153–163.

[52] A. Banerjee, R. Gokhale, S. Bhatnagar, J. Jog, M. Bhardwaj, B. Lefez, B. Hannoyer, S. Ogale, MOF derived porous carbon–Fe_3O_4 nanocomposite as a high performance, recyclable environmental superadsorbent, J. Mater. Chem. 22 (37) (2012) 19694–19699.

[53] P. Horcajada, C. Serre, G. Maurin, N.A. Ramsahye, F. Balas, M. Valletregí, M. Sebban, F. Taulelle, G. Férey, Flexible porous metal-organic frameworks for a controlled drug delivery, J. Am. Chem. Soc. 130 (21) (2008) 6774–6780.

[54] C. Gong, D. Chen, X. Jiao, Q. Wang, Continuous hollow α-Fe_2O_3 and α-Fe fibers prepared by the sol–gel method, J. Mater. Chem. 12 (6) (2002) 1844–1847.

[55] C. Tao, Y. Liu, L. Wang, S. Zhang, Y. Zeng, J. Yuan, J. Ma, W. Dong, C. Liu, S. Luo, Silver phosphate-based Z-Scheme photocatalytic system with superior sunlight photocatalytic activities and anti-photocorrosion performance, Appl. Catal. B 208 (2017) 1–13. Complete.

[56] S.K. Tam, D. Julie, P. Stefania, M. Martin, H. Jean-Pierre, Y. L'Hocine, Physicochemical model of alginate-poly-L-lysine microcapsules defined at the micrometric/nanometric scale using ATR-FTIR XPS, and ToF-SIMS, Biomaterials 26 (34) (2005) 6950–6961.

[57] C. Yu, L. Gou, X. Zhou, N. Bao, H. Gu, Chitosan–Fe3O4 nanocomposite based electrochemical sensors for the determination of bisphenol A, Electrochim. Acta 56 (25) (2011) 9056–9063.

[58] T. Yan, J. Tian, W. Guan, Q. Zheng, W. Li, J. You, B. Huang, Ultra-low loading of Ag_3 PO_4 on hierarchical In_2S_3 microspheres to improve the photocatalytic performance: The cocatalytic effect of Ag and Ag_3PO_4, Appl. Catal. B 202 (2017) 84–94.

[59] R. Liang, F. Jing, L. Shen, N. Qin, L. Wu, MIL-53(Fe) as a highly efficient bifunctional photocatalyst for the simultaneous reduction of Cr(VI) and oxidation of dyes, J. Hazard. Mater. 287 (2015) 364–372.

[60] C. Vimlesh, P. Jaesung, C. Young, L. Jung Woo, H. In-Chul, K.S. Kim, Water-dispersible magnetite-reduced graphene oxide composites for arsenic removal, Acs NANO 4 (7) (2010) 3979–3986.

[61] L. Zhou, W. Zhang, L. Chen, H. Deng, Z-scheme mechanism of photogenerated carriers for hybrid photocatalyst Ag_3PO_4/g-C_3N_4 in degradation of sulfamethoxazole, J. Coll. Interf. Sci. 487 (2017) 410–417.

[62] R. Zheng, L. Li, J. Xie, Y. Zhu, Y. Xie, State of doped phosphorus and its influence on the physicochemical and photocatalytic properties of P-doped Titania, J. Phys. Chem. C 112 (39) (2008) 15502–15509.

[63] C. Fei, Y. Qi, Y. Wang, J. Zhao, D. Wang, X. Li, G. Zhi, W. Hou, Y. Deng, C. Niu, Novel ternary heterojunction photcocatalyst of Ag nanoparticles and g-C_3N_4 nanosheets co-modified $BiVO_4$ for wider spectrum visible-light photocatalytic degradation of refractory pollutant, Appl. Catal. B 205 (2016) 133–147.

[64] Y. Yang, C. Zhang, D. Huang, G. Zeng, J. Huang, C. Lai, C. Zhou, W. Wang, H. Guo, W. Xue, R. Deng, M. Cheng, W. Xiong, Boron nitride quantum dots decorated ultrathin porous g-C_3N_4: Intensified exciton dissociation and charge transfer for promoting visible-light-driven molecular oxygen activation, Appl. Catal. B 245 (2019) 87–99.

[65] W. Wang, P. Xu, M. Chen, G. Zeng, C. Zhang, C. Zhou, Y. Yang, D. Huang, C. Lai, M. Cheng, L. Hu, W. Xiong, H. Guo, M. Zhou, Alkali metal-assisted synthesis of graphite carbon nitride with tunable band-gap for enhanced visible-light-driven photocatalytic performance, ACS Sustain. Chem. Eng. 6 (11) (2018) 15503–15516.

[66] T. Xiao, Z. Tang, Y. Yang, L. Tang, Y. Zhou, Z. Zou, In situ construction of hierarchical WO_3/g-C_3N_4 composite hollow microspheres as a Z-scheme photocatalyst for the degradation of antibiotics, Appl. Catal. B 220 (2018) 417–428.

[67] Y. Liu, J. Kong, J. Yuan, W. Zhao, X. Zhu, C. Sun, J. Xie, Enhanced photocatalytic activity over flower-like sphere Ag/Ag_2CO_3/$BiVO_4$ plasmonic heterojunction photocatalyst for tetracycline degradation, Chem. Eng. J. 331 (2018) 242–254.

[68] Y. Deng, L. Tang, G. Zeng, J. Wang, Y. Zhou, J. Wang, J. Tang, L. Wang, C. Feng, Facile fabrication of mediator-free Z-scheme photocatalyst of phosphorous-doped ultrathin graphitic carbon nitride nanosheets and bismuth vanadate composites with enhanced tetracycline degradation under visible light, J. Coll. Interf. Sci. 509 (2018) 219–234.

[69] Y. Feng, X. Yan, C. Liu, Y. Hong, L. Zhu, M. Zhou, W. Shi, Hydrothermal synthesis of CdS/Bi_2MoO_6 heterojunction photocatalysts with excellent visible-light-driven photocatalytic performance, Appl. Surf. Sci. 353 (2015) 87–94.

[70] F. Guo, W. Shi, W. Guan, H. Huang, Y. Liu, Carbon dots/g-C3N4/ZnO nanocomposite as efficient visible-light driven photocatalyst for tetracycline total degradation, Sep. Purif. Technol. 173 (2017) 295–303.

[71] C. Fei, Y. Qi, X. Li, G. Zeng, D. Wang, C. Niu, J. Zhao, H. An, T. Xie, Y. Deng, Hierarchical assembly of graphene-bridged Ag_3PO_4/Ag/$BiVO_4$ (040) Z-scheme photocatalyst: An efficient, sustainable and heterogeneous catalyst with enhanced visible-light photoactivity towards tetracycline degradation under visible light irradiation, Appl. Catal. B 200 (2017) 330–342.

[72] H. Wang, X. Yuan, H. Wang, X. Chen, Z. Wu, L. Jiang, W. Xiong, G. Zeng, Facile synthesis of Sb_2S_3/ultrathin g-C_3N_4 sheets heterostructures embedded with g-C_3N_4 quantum dots with enhanced NIR-light photocatalytic performance, Appl. Catal. B 193 (2016) 36–46.

[73] C. Liang, C.G. Niu, M. Shen, S.F. Yang, G. Zeng, Controllable fabrication of novel heterojunction composite: AgBr and Ag@Ag_2O co-modified Ag_2CO_3 with excellent photocatalytic performance towards refractory pollutants degradation, New J. Chem. 42 (5) (2018) 3270–3281.

[74] F.A. Sofi, K. Majid, Enhancement of the photocatalytic performance and thermal stability of an iron based metal–organic-framework functionalised by Ag/Ag_3PO_4, Mater. Chem. Front. 2 (5) (2018) 942–951.

[75] Y. Han, H. Shi, C. Bai, L. Zhang, J. Wu, H. Meng, Y. Xu, X. Zhang, Ag_3PO_4-MIL-53 (Fe) composites with visible-light-enhanced photocatalytic activities for Rhodamine B degradation, ChemistrySelect 3 (28) (2018) 8045–8050.